Journal of Sound and Vibration 620 (2026) 119459

Contents lists available at ScienceDirect

Journal of Sound and Vibration

journal homepage: www.elsevier.com/locate/jsvi

Dynamical integrity of synchronous motion for self-synchronizing vibrating screens with two unbalanced exciting rotors

Márton Szabó [*], Ákos Miklós, Giuseppe Habib

Budapest University of Technology and Economics, Department of Applied Mechanics, Műegyetem rkp. 3., Budapest, H-1111, Hungary
MTA-BME Lendület Global Dynamics Research Group, Műegyetem rkp. 3., Budapest, H-1111, Hungary

ARTICLE INFO

Keywords:
Self-synchronization
Vibrating screen
Dynamical integrity
Robustness analysis
Basin of attraction

ABSTRACT

This paper investigates the robustness of self-synchronizing vibratory screens against driving torque differences between the rotors. Synchronous solutions of the mechanical system, which encompasses either a DC motor or an induction motor drive, are first obtained analytically through the averaging method, together with their linear stability properties. Then, numerical validation through direct time integrations confirmed the analytical results. The results indicate that for both motor types, there exists a parameter region, defined in terms of supplied voltages, where a stable synchronous state and a stable non-synchronous state coexist. The analysis of the dynamical integrity of the two types of motions revealed that, for both drives, in regions where synchronized motion is not globally stable, the dynamical integrity of the synchronous motion is relatively low, posing a risk to reliable operation.

1. Introduction

Since the middle of the 20th century, scientists have noticed the inclination of machines driven by two or more eccentric rotors towards self-synchronization [1], which was a known phenomenon ever since Huygens [2] observed it during the anti-phase synchronization of two pendulum clocks. This means that rotors that are not otherwise connected mechanically, for example through gears, tend to still synchronize their motion through the weak coupling of the machine body. One of the prime examples of machines showing this phenomenon are linear vibrating screens, which have two unbalanced shafts rotating in the opposite direction, theoretically creating a translational force excitation on the sieve body. These screens are widely used in various industries like mining, mineral processing or agriculture to separate the material to be processed into multiple grades by particle size. Self-synchronization is often utilized in these applications to lower manufacturing and servicing costs, since this way no connecting mechanical parts or electronic elements are required to synchronize the rotors and ensure the requisite translational motion of the machine body, vital for the separation process. However, this holds the risk that, in the case of substandard design or an unforeseen disturbance, the synchronization of the rotors is not achieved, resulting in unwanted motions on the screen making it impossible to perform the sieving task. As a consequence, a proper understanding and sufficient knowledge about the boundaries of safe operation regarding the stability of the synchronous motion, and its robustness against external perturbations, is needed in order to guarantee that the vibratory machine's design parameters will not cause undesirable dynamical behavior.

The first scientist to thoroughly investigate the phenomenon of self-synchronization was Blekhman [1,3,4], who focused on developing a uniform mathematical theory to systematically study synchronism through the application of the Poincaré–Lyapunov

---

[*] Corresponding author at: Budapest University of Technology and Economics, Department of Applied Mechanics, Műegyetem rkp. 3., Budapest, H-1111, Hungary.

E-mail addresses: marton.szabo@mm.bme.hu (M. Szabó), miklosa@mm.bme.hu (Á. Miklós), habib@mm.bme.hu (G. Habib).

https://doi.org/10.1016/j.jsv.2025.119459
Received 19 May 2025; Received in revised form 11 September 2025; Accepted 11 September 2025

small-parameter approach, and by deriving an integral criterion from variational principles. Later, the stability condition was generalized by Paz and Cole [5] for arbitrary positions of the eccentric rotors using Hamilton's principle. Finally, Wen et al. [6,7] developed the integral averaging method to investigate synchronization between two unbalanced rotors in a far-resonant state from the perspective of driving torque balance, which was improved by Zhao et al. [8,9] by introducing small perturbation parameters. These helped simplify the process of the stability analysis for complex systems, which resulted in a number of papers [10–14] using the aforementioned small parameter averaging method to investigate the stability of eccentric rotor synchronization for two or more exciters. In these studies, the reliability of the method was also proven by comparing it to numerical analysis and experiments. All these features can make the small parameter averaging method a preferred option for analytical investigation of complex mechanical models, where the equations of motion are not necessarily simplified.

The papers listed above only examine the local stability of the synchronous regimes [1]. However, since the investigated systems are mostly nonlinear, the region of the phase space where the desired synchronous motions are attractive can be finite. In other words, a stable synchronous state might coexist with other stable, non-synchronized states; in this case, the system can converge to any of the stable states depending on the initial conditions. The set of initial conditions in the phase space from which the system converges to a particular solution is called basin of attraction. In general terms, the larger the basin of attraction of a solution, the more robust is a steady state against external perturbations, a property typically referred to as dynamical integrity [15] or basin stability [16]. The fact that the basin of attraction can be bounded implicates the need for the study of the synchronizing machine's robustness against large perturbations. In this respect, very few studies analyze the robustness of self-synchronizing machinery. Even bifurcation analyses of these systems, such as those by Wen [6] and Mori et al. [17], are primarily concerned with extending the parameter ranges within which the synchronous regime remains locally stable, without addressing its robustness against external perturbations. The work of Kapitaniak et al. [18] examines the basin of attraction of the different types of synchronization achieved by rotating pendulums on a horizontal beam. However, their analysis considers only variations in the initial angular positions of the rotors, while keeping key parameters, such as driving torque, identical across the rotors. This last assumption is rarely met in industrial settings. Consequently, a more comprehensive investigation of the dynamical integrity of self-synchronizing machines is a necessity.

The identification of a steady-state solution's basin of attraction is not a trivial task. While analytical methods, generally based on Lyapunov functions, are unfeasible for large dimensional systems [19,20], numerical methods are either computationally very expensive [21], or have excessive memory requirements, such as for the cell-mapping method [22,23]. Statistical methods based on Monte Carlo sampling [16] can only slightly reduce the computational cost. Additionally, in order to quantify the dynamical integrity of a system, a so-called dynamical integrity measure should be used, which is a scalar quantification of the dynamical integrity of a system based on the shape and extent of its basin of attraction [15,24,25]. Considering this scenario, in this paper, we use the algorithm proposed by Habib [26], which calculates the local integrity measure (LIM) by iteratively identifying smaller and smaller upper estimates of its real value, bypassing the computation of the basin of attraction. The LIM is defined as the smallest distance between the studied solution and the boundary of its basin of attraction [25]. The used algorithm significantly reduces computational time by exploiting a subdivision of the phase space in cells, which resembles the cell mapping method. The method, initially utilizable only for equilibria, was first extended to time delayed systems in [27], and then generalized to periodic solutions of autonomous and non-autonomous systems in [28]. Since the synchronous motion of a vibrating screener is periodic in nature [3], the dynamical integrity analysis was performed using the algorithm in [28].

This work aims to investigate the robustness of self-synchronizing vibrating screens against driving torque differences between the rotors. This can be a main limiting factor for synchronization [6], making it a critical aspect, as in real applications driving motors always have differences, which are enhanced during usage because of deterioration of parts and their substitution. In practice, often one of the motors is entirely substituted during the lifespan of the machine, leading to significant differences between them. Considering the large forces involved, non-synchronized motions typically lead to unpredictable behavior, which might compromise the integrity and safety of the machine, together with the surrounding workspace, and lead to the destruction of the apparatus. This makes the present research particularly relevant for industrial applications. The analysis not only investigates the stability of synchronized motions against differences of the driving torques, but also examines their dynamical integrity, in order to fully understand the practical reliability of stable solutions. To provide a broad view of the practical implication of the study, both direct current (DC) and induction motors are considered in the analysis.

The remaining part of the paper is organized as follows. In Section 2, the equations governing the dynamics of the mechanical model are derived, both for the DC and for the induction motors. Exploiting the small parameter averaging method of Zhao et al. [8,9], the stability of synchronized motions is investigated in Section 3 concerning variations of the voltage difference between the motors. The stability analysis is then validated numerically. Finally, exploiting the `DynIn` toolbox and the related algorithms developed in [26,28], the dynamical integrity of the stable solutions is investigated in Section 4. A brief discussion about the obtained results, their practical implications, and the limitations of the method are discussed in the concluding section.

2. Mechanical model

In an effort to capture the operational characteristic of a self-synchronizing vibrating screen, a simplified mechanical model is presented in Fig. 1. We consider a vibrating screen having the rotors' axes perpendicular to the motion of the material on the sieve, with rotors rotating in opposite directions. A planar model is sufficient to describe the system's dynamics.

The machine body is modeled as a rigid body with mass M and rotational inertia J around the z-axis. The unbalanced rotors are taken into account as concentrated masses m_1 and m_2 with eccentricity e_1 and e_2, respectively. Both of them are driven by electric

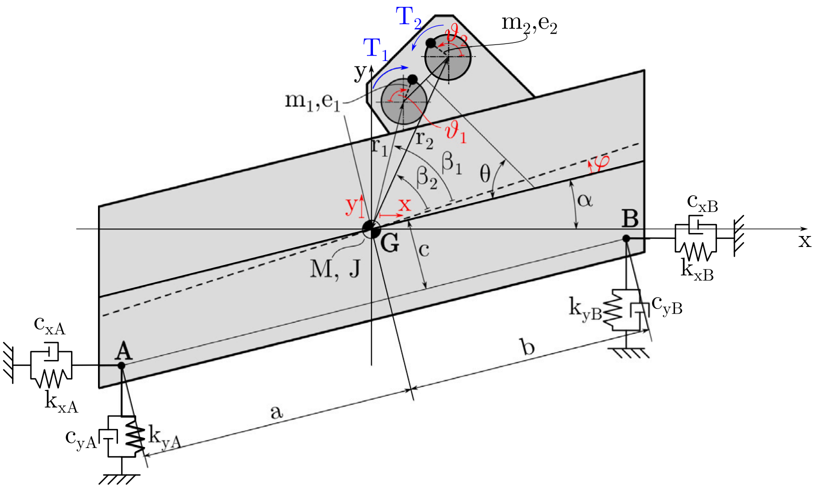

Fig. 1. Mechanical model of the self-synchronizing system.

motors, which are modeled through their driving torques. In addition, the rigid machine body is connected to the foundation through supporting springs with stiffnesses $k_{x\mathrm{A}}$, $k_{x\mathrm{B}}$, $k_{y\mathrm{A}}$, and $k_{y\mathrm{B}}$, and damping coefficients $c_{x\mathrm{A}}$, $c_{x\mathrm{B}}$, $c_{y\mathrm{A}}$, and $c_{y\mathrm{B}}$. The distance between the center of mass **G** of the vibrating body and the supporting springs are defined by a, b, and c, and the inclination angle of the machine at rest is α, as illustrated in Fig. 1. The placement of the eccentric rotors is identified by their polar coordinates from the center of mass, i.e., r_1, r_2, β_1, and β_2.

The differential equations governing the dynamics of the system are derived through the Lagrangian equation of the second kind, for which generalized coordinates are needed. They are chosen as the displacement of the center of mass **G** in x- and y-directions, the swing angle of the machine body φ, and the phase angles of the rotors ϑ_1 and ϑ_2. As a result, we get the following generalized coordinate vector: $\mathbf{q} = [x, y, \varphi, \vartheta_1, \vartheta_2]^T$. Thus, the kinetic energy of the system can be formulated as:

$$\mathcal{T} = \frac{1}{2}M\left(\dot{x}^2 + \dot{y}^2\right) + \frac{1}{2}J\dot{\varphi}^2 + \sum_{i=1}^{2}\frac{1}{2}m_i v_i^2, \tag{1}$$

where v_i are the velocities of the unbalanced masses, and their squares can be written as:

$$v_i^2 = \left(\dot{x} - r_i\dot{\varphi}\sin(\beta_i + \alpha + \varphi) \pm e_i\dot{\vartheta}_i\sin\vartheta_i\right)^2 + \left(\dot{y} + r_i\dot{\varphi}\cos(\beta_i + \alpha + \varphi) + e_i\dot{\vartheta}_i\cos\vartheta_i\right)^2 \quad i = 1, 2. \tag{2}$$

The potential energy of the system $\mathcal{U}$ and the dissipation energy function $\mathcal{D}$ are constructed in the following way:

$$\mathcal{U} = \frac{1}{2}k_{xA}x_A^2 + \frac{1}{2}k_{xB}x_B^2 + \frac{1}{2}k_{yA}y_A^2 + \frac{1}{2}k_{yB}y_B^2 \tag{3}$$

$$\mathcal{D} = \frac{1}{2}c_{xA}\dot{x}_A^2 + \frac{1}{2}c_{xB}\dot{x}_B^2 + \frac{1}{2}c_{yA}\dot{y}_A^2 + \frac{1}{2}c_{yB}\dot{y}_B^2, \tag{4}$$

where the displacements of the springs and their time derivatives are provided in Appendix A. The Lagrangian equation of the second kind is expressed according to

$$\frac{\mathrm{d}}{\mathrm{d}t}\frac{\mathrm{d}\mathcal{T}}{\mathrm{d}\dot{q}_k} - \frac{\mathrm{d}\mathcal{T}}{\mathrm{d}q_k} + \frac{\mathrm{d}\mathcal{D}}{\mathrm{d}\dot{q}_k} + \frac{\mathrm{d}\mathcal{U}}{\mathrm{d}q_k} = Q_k^* \qquad k \;= 1 \dots 5 \tag{5}$$

from which the equations of motion are derived, as illustrated in Appendix A.

In the equation, the generalized forces are the torques acting on the rotors, i.e., $Q_4^* = n_m T_1$ and $Q_5^* = n_m T_2$, where n_m is the number of driving motors on one shaft, and T_1 and T_2 are the driving torque of the motors. In this paper, as stated in the introduction, we consider two exciting motor models, a DC and an induction motor model. In the former case, the driving torque can be expressed as [17,29]:

$$T_i^{\mathrm{DC}} = \frac{K_t}{R_a}U_i - \left(\frac{K_t K_E}{R_a} + c_i\right)\dot{\vartheta}_i, \tag{6}$$

where K_t, K_E, and R_a are the torque constant, voltage constant and the armature resistance, respectively, while U_i is the voltage supplied to the motors, and c_i is the resistance coefficient of viscous friction. Similarly, according to Chapman [30], the model of an induction motor can be written as:

$$T_i^{\mathrm{AC}} = \frac{3}{\omega_s}\cdot\frac{\frac{R_r}{s_i}}{\left[R_s\left(\frac{L_m}{L_s+L_m}\right)^2 + \frac{R_r}{s_i}\right]^2 + (L_s + L_r)^2}\cdot\left(\frac{L_m}{L_s + L_m}\right)^2\cdot U_i^2 - c_i\dot{\vartheta}_i, \tag{7}$$

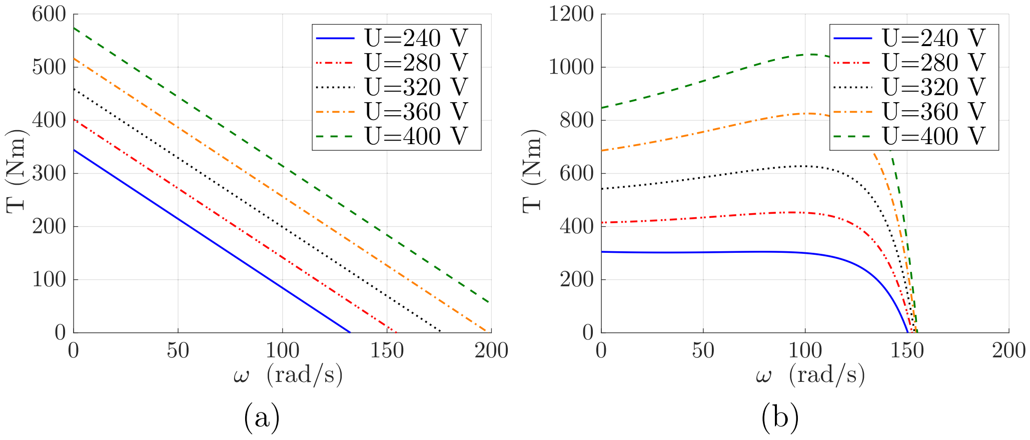

Fig. 2. Motor characteristics with the change of the supplied voltage: (a) DC motor described in Table 2. (b) Induction motor with parameters in Table 3.

where $s_i = (\omega_s - \dot{\vartheta}_i)/\omega_s$ is the slip of the motor, with ω_s synchronous speed. R_s, L_s and R_r, L_r are the resistance and inductance for the stator and the rotor, respectively, while L_m is the magnetizing reactance. In this case too, U_i is the supplied voltage and c_i is the frictional resistance coefficient. For both types of driving motors, we assume that the motors driving the two rotors are identical. The motor characteristics of the two drives can be seen in Fig. 2, with the parameters in Tables 2 and 3. The nominal voltage of the motors are 400 V in both cases, which corresponds to an angular velocity of $\omega \approx 150$ rad/s at the working point, yielding a nominal power of $P \approx 19.5$ kW. It is important to note that the static torque–speed slopes of the two motor types differ significantly: for the DC motor drive the slope is $\mathrm{d}T_i^{\mathrm{DC}}/\mathrm{d}\dot{\vartheta}_i = -2.99$ Nm/rad/s, while for the induction motor drive, it is $\mathrm{d}T_i^{\mathrm{AC}}/\mathrm{d}\dot{\vartheta}_i = -46.04$ Nm/rad/s. In practical engineering contexts, however, driving motors are selected based on nominal power and rotational frequency, rather than static slope. Therefore, this basis for comparison is considered more relevant from an application-oriented perspective.

It is worth mentioning that conventionally induction motors are variable-frequency drives, meaning that the input is a frequency signal rather than supplied voltage. However, for the sake of comparison between the two motor classes, also for the induction motor we considered the voltage as the input variable. It should also be noted that, during workplace accidents, the loss of supplied voltage can be a leading source of the problem, making the voltage a practical input variable when the safety and robustness of the system is being assessed. A good example of a similar incident is the event that led to the discovery of self-synchronization of rotating exciters, as described in [1]. Furthermore, even if induction motors are a preferable choice for industrial applications, the investigation of direct current motor drives should not be neglected from an academic viewpoint [17]. This justifies the effort to examine both types of drives for self-synchronization.

3. Stability analysis

The stability of a mechanical model similar to the one described in Section 2 was already investigated by Peng et al. [12]. In their paper, they used lumped stiffness and damping terms during the derivation of their model, which encompassed an induction motor drive with identical unbalanced rotors. They performed analytical calculations on the local stability of the synchronous motion using the small parameter averaging method of Zhao et al. [8]. Following the computational steps done in their study, the stability chart of the synchronized motion can be calculated. First, the motion of the screen body and the rotors is separated, and the approximate steady-state solutions of the machine body in the vertical, horizontal and swing directions are computed from (A.9)–(A.11) in Appendix A, which can be written in the following form, as functions of the rotors angular velocities and phase angles:

$$x = e_1 \mu_x \eta_1 \cos(\vartheta_1 - \delta_x) - e_2 \mu_x \eta_2 \cos(\vartheta_2 - \delta_x) \tag{8}$$

$$y = e_1 \mu_y \eta_1 \sin(\vartheta_1 - \delta_y) + e_2 \mu_y \eta_2 \sin(\vartheta_2 - \delta_y) \tag{9}$$

$$\varphi = M_t \frac{e_1 r_1}{J_t} \mu_\varphi \eta_1 \sin(\vartheta_1 - \alpha - \beta_1 - \delta_\varphi) + M_t \frac{e_2 r_2}{J_t} \mu_\varphi \eta_2 \sin(\vartheta_2 + \alpha + \beta_2 - \delta_\varphi), \tag{10}$$

where the dimensionless parameters, with indexes $i = 1, 2$ and $j = x, y, \varphi$ are expressed as:

$$\begin{array}{lll} M_t = M + \sum m_i, & J_t = J + \sum m_i r_i^2, & \eta_i = \dfrac{m_i}{M_t}, \\ \omega_{n,x} = \sqrt{\dfrac{k_{xA} + k_{xB}}{M_t}}, & \zeta_x = \dfrac{c_{xA} + c_{xB}}{2\sqrt{M_t k_x}}, & \lambda_x = \dfrac{\overline{\omega}_m}{\omega_{n,x}}, \\ \omega_{n,y} = \sqrt{\dfrac{k_{yA} + k_{yB}}{M_t}}, & \zeta_y = \dfrac{c_{yA} + c_{yB}}{2\sqrt{M_t k_y}}, & \lambda_y = \dfrac{\overline{\omega}_m}{\omega_{n,y}}, \\ \omega_{n,\varphi} = \sqrt{\dfrac{a^2 k_{yA} + b^2 k_{yB}}{J_t}}, & \zeta_\varphi = \dfrac{a^2 c_{yA} + b^2 c_{yB}}{2\sqrt{J_t(a^2 k_{yA} + b^2 k_{yB})}}, & \lambda_\varphi = \dfrac{\overline{\omega}_m}{\omega_{n,\varphi}}, \\ \delta_j = \arctan\left(\dfrac{2\zeta_j \lambda_j}{1 - \lambda_j^2}\right), & \mu_j = \dfrac{\lambda_j^2}{\sqrt{(1 - \lambda_j^2)^2 + (2\zeta_j \lambda_j)^2}}, & \end{array} \tag{11}$$

Then, the rotational angle of the rotors is assumed to be $\vartheta_i = \vartheta \pm \xi$, where ϑ is the average phase angle of the rotors and 2ξ is the phase difference. This way, since the average angular velocity $\omega_m(t) = \dot{\vartheta}(t)$ is periodic, its mean value can be written as:

$$\overline{\omega}_m = \frac{1}{T} \int_t^{t+T} \dot{\vartheta}(\tau)\, \mathrm{d}\tau = \text{constant}. \tag{12}$$

After that, we can introduce the time dependent parameters ε_1 and ε_2, which are the instantaneous variation coefficients in $\dot{\vartheta}$ and $\dot{\xi}$:

$$\dot{\vartheta} = (1 + \varepsilon_1)\overline{\omega}_m, \tag{13}$$

$$\dot{\xi} = \varepsilon_2 \overline{\omega}_m. \tag{14}$$

Following these definitions, the expressions with these parameters are substituted back into the differential equations of the rotors, which are Eqs. (A.12) and (A.13) in Appendix A, together with the accelerations and velocities of each coordinate of the machines body calculated from (8)–(10). The equations of the driving torques (6) and (7) are also added in the form $T_i = T_{i0} - k_i(\varepsilon_1 \pm \varepsilon_2)$, after which the two differential equations are integrated over one period of the motion: $\vartheta \in [0,\ 2\pi]$. It can be assumed that the variation of ε_1, ε_2 and ξ are small and periodic, so they can be replaced by their average values in the equations [8]. This way, after neglecting the higher order terms, we calculate the sum and difference of the two equations. By adding Equation (14) to this system of equations, the equation of frequency capture can be obtained:

$$\mathbf{A}\dot{\boldsymbol{\varepsilon}} = \mathbf{B}\boldsymbol{\varepsilon} + \mathbf{u}, \tag{15}$$

where $\boldsymbol{\varepsilon} = [\overline{\varepsilon}_1, \overline{\varepsilon}_2, \overline{\xi}]^T$, while $\mathbf{A}$, $\mathbf{B}$, and $\mathbf{u}$ are shown in Appendix B.

When the system is in a synchronous state, the average variations of the velocities of the mean phase angle and the phase difference are assumed to be zeros, and the phase difference to be a constant value: $\overline{\varepsilon}_1 = \overline{\varepsilon}_2 = 0$, $\overline{\xi} = \overline{\xi}_0 =$ constant. With these assumptions, the synchronization condition can be calculated in the form: $|T_D| \leq T_S$, where T_D is the residual out torque [12] between the two motors and T_S is the synchronous torque.

$$T_D = T_{10} - T_{20} - (f_1 - f_2)\overline{\omega}_m - \frac{M_t \overline{\omega}_m^2}{2}\left(\eta_1^2 e_1^2 W_{ss1} - \eta_2^2 e_2^2 W_{ss2}\right) \tag{16}$$

$$T_S = M_t \eta_1 \eta_2 e_1 e_2 \overline{\omega}_m^2 W_{cs}. \tag{17}$$

Full expressions of the parameters in the above equations are provided in Appendix B. The system in (15) can be linearized around the $\overline{\varepsilon}_1 = \overline{\varepsilon}_2 = 0$, $\overline{\xi} = \overline{\xi}_0$ point, which allows computing its stability through the Routh–Hurwitz criterion. Using this method, the stability boundary related to supplied voltage difference for the motors can be rapidly determined for different mean voltages. The process is the same for both the DC and the induction motor, only the driving torque models need to be changed. With the described analytical method, the local stability of the synchronous motion can be swiftly computed, which makes it suitable for parametric studies as well. For example, Fig. 3 illustrates the stability boundary in the plane of the voltage difference U_{diff} and the mean of the supplied voltages U_{avg} for different θ inclination angles of the excitation (Fig. 1). In other words, while $r_1 \cos\beta_1 + r_2 \cos\beta_2 = 0$ is always satisfied, the angle

$$\theta = \arctan\left(\frac{r_1 \sin\beta_1 - r_2 \sin\beta_2}{r_1 \cos\beta_1 - r_2 \cos\beta_2}\right) \tag{18}$$

was changed from an initial $\theta = 90°$ to $\theta = 45°$. The results indicate a reduction of the stable region for reducing angle θ. As the main focus of this study is the global stability of synchronous solutions, and because parametric studies have already been done on very similar systems [12], the analysis of the system's local stability in relation to geometric parameters is not further investigated here.

The local stability of the synchronized state was validated using direct numerical simulations, where, for each U_{avg} value, the voltage difference U_{diff} is first increased step-by-step, and then decreased. For each U_{avg} value, a simulation has been run until the

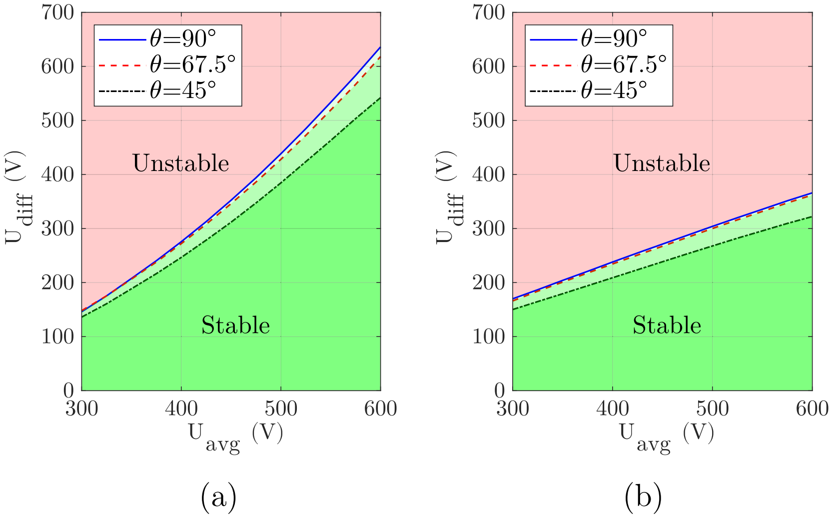

Fig. 3. Boundary of stability for different θ inclination angles of the excitation: (a) Direct current motor drive. (b) Induction motor drive. Parameter values are indicated in Tables 1–3.

Table 1

Parameters of the screen body.

$m_{1,2}$	M	$e_{1,2}$	J	α	a	b	c
(kg)	(kg)	(m)	(kgm^2)	(°)	(m)	(m)	(m)
300	25 000	0.2	60 000	0	2	2	0.3
r_1	r_2	β_1	β_2	k_x	k_y	c_x	c_y
(m)	(m)	(°)	(°)	$(\frac{\text{kN}}{\text{mm}})$	$(\frac{\text{kN}}{\text{mm}})$	$(\frac{\text{kNs}}{\text{m}})$	$(\frac{\text{kNs}}{\text{m}})$
0.25	0.25	180	0	2	5	40	80

Table 2

Parameters of the DC motors.

n_m	(-)	2
R_a	(Ω)	4.494
K_t	(Nm/A)	3.224
K_E	(V/rad/s)	4.207
$c_{1,2}$	(Nms/rad)	1.6

Table 3

Parameters of the induction motors.

n_m	(-)	2
L_m	(H)	0.03
L_s	(H)	0.008
L_r	(H)	0.008
R_r	(Ω)	0.4
R_s	(Ω)	1
ω_s	(rad/s)	157.08
$c_{1,2}$	(Nms/rad)	1.6

steady-state condition is reached. The initial conditions for each simulation correspond to the last state of the previous simulation, in order to provide a sort of continuation thanks to the small U_{diff} steps.

As shown in Fig. 4, numerical results confirm analytical ones, showing that the synchronous state is stable for large differences in the supplied voltages. This was obtained during the “sweep up” process, when U_{diff} was increased from zero until it reached the stability boundary. However, when the U_{diff} is decreased during the “sweep down”, starting from the initially non-synchronous state, results illustrated that a non-synchronous quasiperiodic motion exists and is stable down to very small U_{diff} values. This indicates that the stable synchronous and non-synchronous motions coexist for a large U_{diff} range. We note that a non-synchronous state implies that the angular velocities do not match, leading to undesired behaviors. It is also worth noting that the simulated

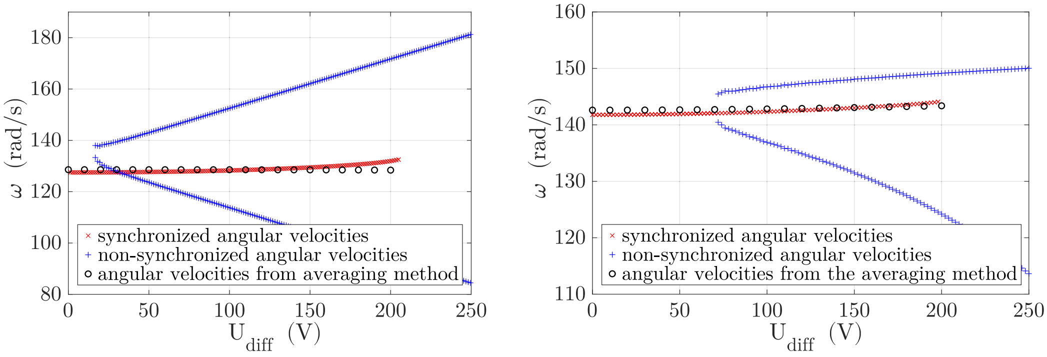

(a) (b)

Fig. 4. Synchronous and non-synchronous angular velocities of the rotors during the step-by-step increase and decrease of the supplied voltage difference for $U_{avg} = 350$ V average voltage value, the former being validated by the analytical results of the averaging method: (a) DC motor drive. (b) Induction motor drive. Used parameters are indicated in Tables 1–3.

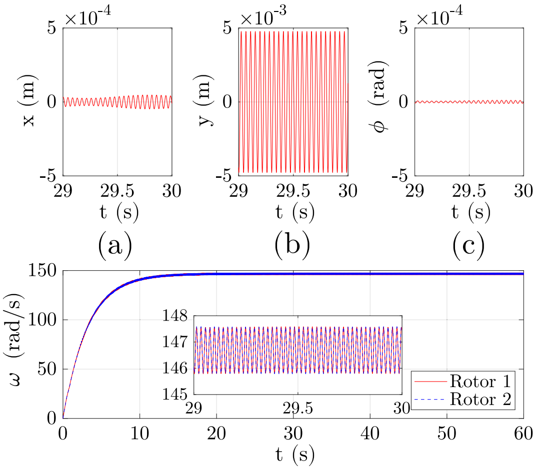

(d)

Fig. 5. Example time series data of the synchronous motion of a DC motor driven vibrating screen, with supplied voltages: $U_1 = 420$ V and $U_2 = 380$ V. Parameters are provided in Tables 1 and 2. (a) Horizontal displacement. (b) Vertical displacement. (c) Swing angle. (d) Angular velocities of the rotors.

synchronous angular velocities correspond well to the analytical results. The parameter values of the machine used in the simulations are provided in Table 1, while the parameter values for both the direct current and induction motors are specified in Tables 2 and 3, respectively. These parameters are defined, so that the motors are similar to the MP160L DC motor [31] and the M3BP 225SMA, a 4 pole induction motor [32]. Their characteristics can be seen in Fig. 2.

This result implies that, for a certain set of supplied voltage pairs, there exist a stable synchronous solution, like the time series shown in Fig. 5, while for the same input voltages but with different initial condition the stable solution is a non-synchronous one, like the one in Fig. 6. This results in the existence of a range of supplied voltage difference between the driving motors, where the stability of the synchronous state is limited [29], because there is also a stable non-synchronous solution. It is worth noting that the motion observed in Fig. 6 resembles a beating response, which, as some publications on self-excited systems have already pointed out [33,34], might correspond to modal synchronization. However, in the present case, since the system is externally forced by the driving motors, the beating behavior is due to the excitation of the rotors, and not internal energy exchanges between oscillators. By applying the same method on a range of supplied voltage values described by their average value and difference, the stability map of the vibrating screens can be derived for both exciting motor cases. The stability maps of the system excited by DC motors and induction motors can be seen in Fig. 7. The results show the same behavior, where, apart from the areas where the synchronous regime is globally stable or unstable, there exists a third range, where both a stable synchronous and a stable non-synchronous state coexist.

The numerical results of the stability chart are validated by analytical calculations done by the use of the small parameter averaging method as well; however, the analytical method can be applied only to the synchronous motion, while the stable region

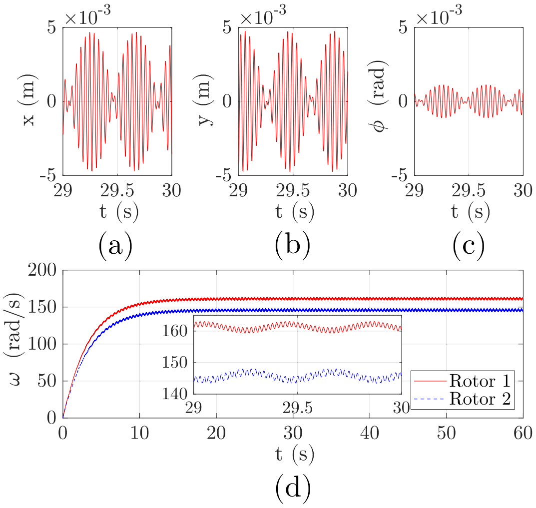

Fig. 6. Example time series data of the non-synchronous motion of a DC motor driven vibrating screen, with supplied voltages: $U_1 = 420$ V and $U_2 = 380$ V (same as in Fig. 5 but with different initial conditions). Parameters are provided in Tables 1 and 2. (a) Horizontal displacement. (b) Vertical displacement. (c) Swing angle. (d) Angular velocities of the rotors.

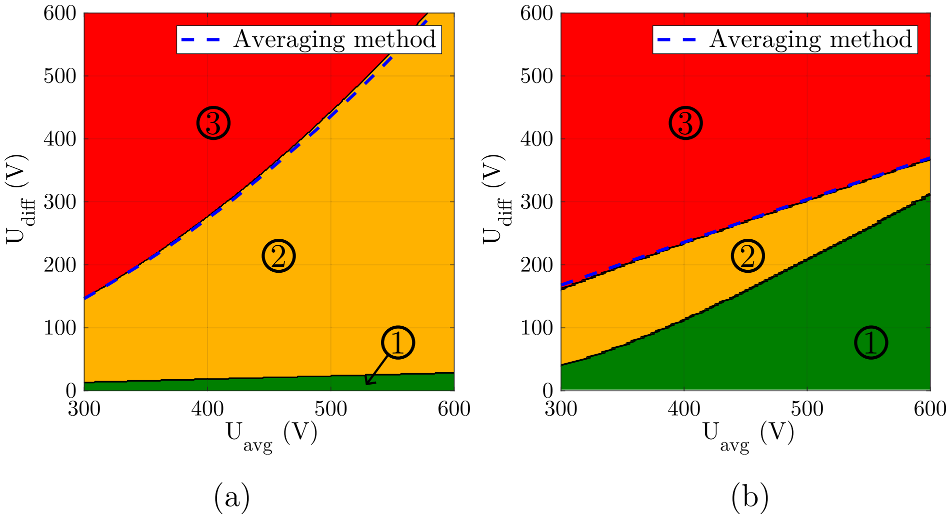

Fig. 7. Stability maps, with area ① indicating the supplied voltage range, where the synchronous state is globally stable, in area ③ no stable synchronous motion exists, and in area ② the synchronous and non-synchronous stable motions coexist: (a) DC motor model. (b) Induction motor model. (For interpretation of the references to color in this figure legend, the reader is referred to the web version of this article.)

of the non-synchronous state is obtained only numerically. This means that the boundary of the region where the synchronous motion is globally stable can only be approximated using numerical methods; nonetheless, its existence is evidently visible as shown in Fig. 8, where it is clear by the behavior of the phase difference that, when the synchronous solution is globally stable, it will always converge to a constant phase difference with small variance, even if perturbations are large enough to initially create rotor velocities with substantial difference. In the other case, when it is only locally stable, large enough perturbations will force the solution to become non-synchronous. As can be seen in Fig. 7, the machine with the DC motor drive has only a small area where the synchronous regime is globally stable, while the range of supplied voltage pairs where it is only locally stable is far larger than in the case of an induction motor drive. Additionally, even though for induction motors the locally stable region is smaller than for the DC motor, the globally stable region of synchronous motion is wider.

Although the difference in the extent of the globally and locally stable range is clear between the DC motors and the induction motors, in order to evaluate the practical usability of the synchronized motion in the bistable region, its dynamical integrity must be computed. This will allow the evaluation of the synchronous solution's robustness against perturbations.

It is also important to emphasize that our decision to compare driving motor types based on equal nominal power rather than equal static slope is justified, in the context of the averaging method. The synchronization condition is given by: $|T_D| \leq T_S$, where

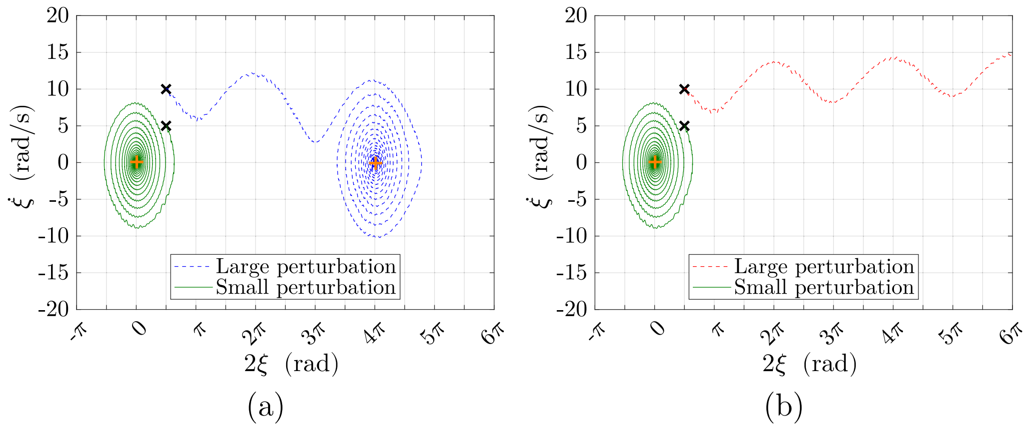

(a) (b)

Fig. 8. Simulation results representing the response of DC motor driven screen, with parameters in Tables 1, 2, and: $U_{\mathrm{avg}} = 400$ V. (a) System in the globally stable parameter region: $U_{\mathrm{diff}} = 4$ V. (b) The synchronous motion is only locally stable: $U_{\mathrm{diff}} = 40$ V.

T_D is a function of the driving torque difference, while the synchronous torque T_S only depends on the angular velocity of the system and the parameters of the screen, as defined in (16)–(17). This formulation implies that the more the torques of the motors depend on the supplied voltage, the smaller the stable region of the synchronous motion will be [8], since the torque difference will increase faster with the voltage difference. The dependence of motor torque on supply voltage can be expressed as:

$$\frac{\mathrm{d}T_i^{\mathrm{DC}}}{\mathrm{d}U_i} = \frac{K_t}{R_a} \tag{19}$$

$$\frac{\mathrm{d}T_i^{\mathrm{AC}}}{\mathrm{d}U_i} = \frac{6L_m^2 R_r U_i}{(L_m+L_s)^2(\omega_s-\dot{\vartheta}_i)\left(\left(\frac{L_m^2 R_s}{(L_m+L_s)^2}+\frac{R_r\omega_s}{\omega_s-\dot{\vartheta}_i}\right)^2+(L_r+L_s)^2\right)} \tag{20}$$

For the parameter sets listed in Tables 2 and 3, these values are $\mathrm{d}T_i^{\mathrm{DC}}/\mathrm{d}U_i = 1.434$ Nm/V for the DC motor drive and $\mathrm{d}T_i^{\mathrm{AC}}/\mathrm{d}U_i = 1.864$ Nm/V for the induction motor drive, indicating that they are comparable with respect to dynamical integrity. Conversely, if the DC motor parameters are artificially adjusted such that its static torque–speed slope matches that of the induction motor, the voltage sensitivity becomes $\mathrm{d}T_i^{\mathrm{DC}}/\mathrm{d}U_i = 9.118$ Nm/V, which renders the two drives incomparable in terms of robustness in the bistable region.

When the system operates in the synchronized regime, the rotor angular velocities remain close to the designated operating point, where the use of the static torque–speed characteristic is valid, thus this interpretation for the variation of the stability boundary works. In contrast, during non-synchronous motion, when the rotors rotate at differing angular velocities, the system deviates significantly from the operating point. As a result, the static characteristic becomes an inadequate representation of the motors' behavior in this regime. Consequently, the differences observed in the stability boundaries of the non-synchronous state between the two motor types cannot be fully explained using this framework alone, which is another reason why robustness analysis in the bistable region is crucial for a more comprehensive understanding of the system's behavior.

4. Dynamical integrity calculation

In the effort of approximating the robustness of the system with respect to external perturbations, it is essential to assess the dynamical integrity of the synchronous regimes within the bistable region (orange regions, marked with ② in Fig. 7). Conversely, in the parameter space where the synchronous motion is unstable (red regions, ③ in the figure), the dynamical integrity is reduced to zero because of the instability, while in the globally stable region (green regions, ①), the dynamical integrity is theoretically infinite (unless other undetected solutions exist). The foundation of the algorithm employed for the dynamical integrity analysis was originally proposed by Habib in [26]; while the specific approach applied in this study to analyze the dynamical integrity of periodic solutions—such as the synchronized motion of the vibrating screen—was developed by Patko and Habib in [28].

The utilized iterative method relies on direct numerical simulations and the characterization of each trajectory as converged to or diverged from the desired periodic solution, where each simulation corresponds to an iteration step. The computation process involves discretizing the phase space into a finite number of cells, each corresponding to a state entity, used for trajectory classification. Specifically, if a trajectory reaches the desired periodic orbit, the corresponding cell and any other cells it traverses are designated as converging cells, whereas those leading to divergence are classified as diverging cells. This classification scheme enables rapid exploration of the phase space, as once a trajectory intersects a previously classified cell, its behavior can be inferred without further computation. Each time a diverging trajectory is encountered, the LIM is computed as the minimal distance between the synchronized motion and the diverging trajectory. The LIM value is updated if the newly calculated value is smaller than the one computed at previous iterations. The selection of the initial conditions of each trajectory is based on a bisection

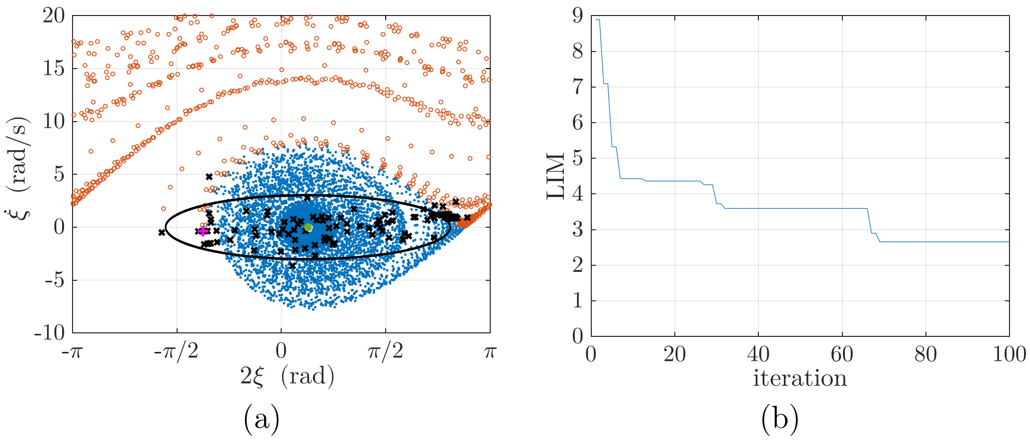

Fig. 9. Process of the LIM calculation: (a) The phase difference and its velocity is shown from the phase space. (b) Trend of the LIM value. (For interpretation of the references to color in this figure legend, the reader is referred to the web version of this article.)

scheme, which initially relies on random guesses. This process aims at identifying trajectories as close as possible to the basin of attraction boundaries, which are the most informative with respect to the solution's dynamical integrity. Since the phase space is not entirely investigated, the computed LIM value is an overestimation of the real one. However, this trade-off is necessary to maintain computational efficiency.

Implementation of the method requires the specification of several parameters, including the boundaries of the investigated region in phase space, the number of iterations, and the number of discretized cells along each coordinate axis. An initial estimate for a point of the target solution is then provided, enabling the algorithm to compute the corresponding periodic orbit. Subsequently, the iterative procedure is initiated.

In our investigation, the desired solution is the synchronized motion of the vibrating screen, which we have already numerically calculated in Section 3, during the stability assessment for each supplied voltage pair. The LIM computing algorithm employed 100 iteration steps for each voltage pair. The phase space was discretized in 1501 cells along each dimension of the system. Given that the simulated system derived from the mechanical model is 10 dimensional, this results in a total of 1501^{10} cells. We remark that the algorithm does not require to investigate all cells, otherwise memory requirements would make the computation unfeasible. Weight coefficients were also introduced for the calculation of the distance in the phase space to balance out the differences of the coordinate. This is an essential step for the definition of the Euclidean distance in the anisotropic phase space of the system, which encompasses angles, distances, and their time derivatives. A thorough discussion on the topic is available in [26].

To enable meaningful comparisons between numerical simulations and analytical approximations derived via the small-parameter averaging method, the two phase angle coordinates of the rotors, ϑ_1 and ϑ_2, are reformulated in the numerical simulations as ϑ, representing the average phase angle of the rotors, and 2ξ, denoting the phase difference between them. Their corresponding time derivatives are denoted by ω_ϑ and ω_ξ, respectively, to clearly indicate their physical interpretation as the mean angular velocity and the angular velocity difference of the rotors.

The results of the dynamical integrity analysis for an illustrative case is depicted in Fig. 9, where the projected periodic orbit is represented by green dots. However, since in this section of the phase space the periodic solution is much smaller than the basin of attraction, it appears as a single dot. The black line marks the so-called hypersphere of convergence, which is a hypersphere with a radius equal to the computed LIM value, centered at the closest point of the periodic solution to any diverging trajectory. The black crosses indicate the initial conditions of the performed simulations, while the magenta + marks the closest point of the diverging trajectory to the desired solution, from which the final LIM is calculated. The blue dots and orange circles indicate points of converging and diverging trajectories, respectively, mapped to the $[-\pi, \pi]$ phase difference interval. We note that points in Fig. 9a are projected on the 2-dimensional space from the original 10-dimensional space, except for the hypersphere of convergence, for which a section is represented. Accordingly, the magenta + does not lie exactly on the hypersphere of convergence, and the orange dots might appear within the hypersphere. Fig. 9b displays the evolution of the LIM value as the iteration progresses. After only a few iterations (9 in this case), the algorithm already provides a good estimate of the LIM value, which is then refined in the subsequent ones. This implies that, if only a rough estimate of the LIM is required, a few iteration steps are generally enough.

Since the analysis is restricted to a finite portion of the phase space, indicated in Table 4, there exists an upper bound for the LIM. This upper limit is determined by the distance between the boundary of the examined phase space region and the periodic solution. Consequently, even in cases where the system exhibits global stability, the obtained estimate of the LIM remains finite. In this study, the maximum attainable value is approximately 9. It is important, however, to point out the fact that interpreting the LIM value in itself is not easy, because its value is inherently dependent on several factors. These include the extent of the observed phase space region, the weight coefficients utilized in the computation of distances and the coordinates used in the governing equations. Nevertheless, if we take into account this upper limit value and 0, which corresponds to the loss of stability, we can approximately

Table 4
Boundaries of the investigated phase space during the robustness calculations.

x	$\dot{x}$	y	$\dot{y}$	φ	$\dot{\varphi}$	ϑ	$\dot{\vartheta}$	ξ	$\dot{\xi}$
(m)	$(\frac{\mathrm{m}}{\mathrm{s}})$	(m)	$(\frac{\mathrm{m}}{\mathrm{s}})$	(rad)	$(\frac{\mathrm{rad}}{\mathrm{s}})$	(rad)	$(\frac{\mathrm{rad}}{\mathrm{s}})$	(rad)	$(\frac{\mathrm{rad}}{\mathrm{s}})$
± 0.1	± 5	± 0.1	± 5	± 0.5	± 5	$\pm 2\pi$	$\omega_m \pm 20$	$\pm 2\pi$	± 20

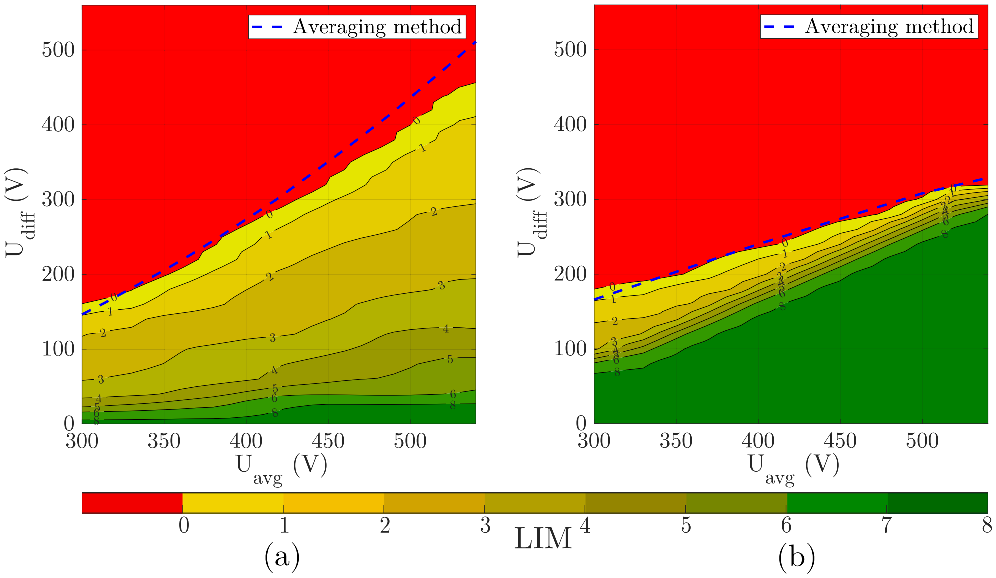

Fig. 10. The LIM values for different supplied voltage pairs in the case of vibrating screens excited by: (a) DC motors. (b) Induction motors.

define robust/safe regions. To ensure that this definition of a safe region is realistic, the boundaries of the phase space must be chosen in a way that the values outside it should not have to be considered from a practical perspective. Indeed, the LIM's trend in the parameter space is much more informative than its value for a specific condition, as the trend provides a clear understanding of the effect of parameter values' variations on the robustness, a critical parameter for safe engineering design.

The results of the robustness analysis are visualized by mapping the LIM values onto the stability diagrams of the systems excited by the DC and induction motors, as shown in Fig. 10. Additionally, Fig. 11 presents cross-sections of the robustness diagram, illustrating the decline in the LIM as the supplied voltage difference increases, for fixed average voltage values. As observed, the self-synchronizing vibrating screen driven by DC motors exhibits an extensive region, in which the synchronous motion is only locally stable. Moreover, increasing the supplied voltage differences, as soon as the system enters the bistable region, the LIM value very rapidly decreases. This finding implies that operating within this region should be avoided, as even minor perturbations may lead to undesired dynamical phenomena. Even when applying a LIM threshold of 4 as a criterion for robustness—interpreted as requiring close to half of the investigated phase space to remain stable—the resulting region for the DC motor-driven system's diagram is still significantly smaller than the globally stable region available for the system driven by induction motors. This further reinforces the advantage of induction motor drives in ensuring stable and reliable operation under varying external conditions. It should be emphasized that, although the globally stable region is larger for systems driven by induction motors, the bistable region remains unsuitable for long-term operation due to the rapid decline of the LIM. Overall, large torque differences should be avoided in case of DC motor drives, to prevent operations in the bistable region, where external perturbations could induce non-synchronous behavior. In contrast, systems driven by induction motors exhibit larger robustness, and even significant supplied voltage differences can still provide synchronous motion with reliable stability.

In order to illustrate the relation between the calculated LIM values and the actual size of the basin of attraction it is intended to characterize, we computed the basin of attraction for the synchronous motion for some specific cases using the traditional method. This involves superimposing a grid over the phase space and initiating simulations from each grid cell. The resulting trajectories were subsequently classified individually as either convergent or divergent. For obvious computational time and memory constraints, only a two-dimensional sections of the 10-dimensional basin of attraction were computed. Variations of initial conditions involved the phase difference and angular velocity difference between the rotors, while the other initial conditions values remained zero at all time. The obtained sections of the basins of attraction are illustrated in Fig. 12.

The procedure was completed for both types of drives for an average supplied voltage value of $U_{\mathrm{avg}} = 400$ V, and for two different voltage difference values: $U_{\mathrm{diff}} = 40$ V and $U_{\mathrm{diff}} = 200$ V. Planar sections of the periodic orbits representing the desired synchronous

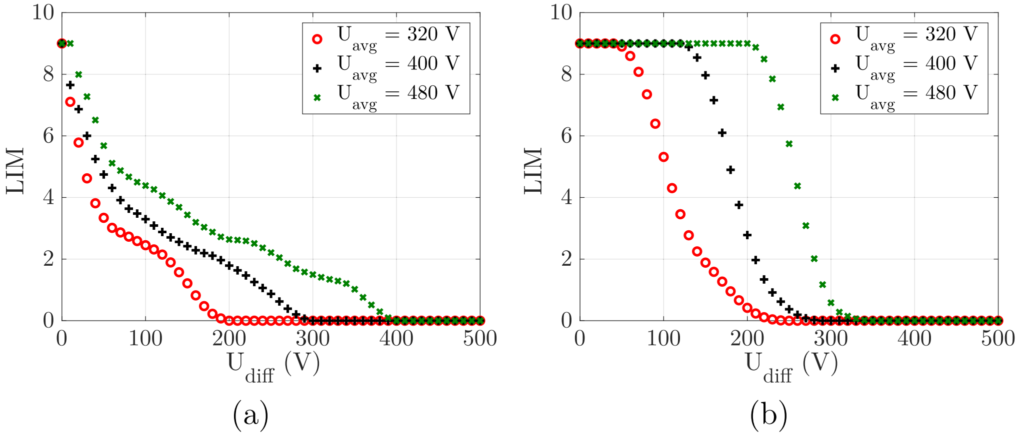

Fig. 11. Variations of the LIM with the increase of supplied voltage difference for different average voltage values: (a) DC motor drive. (b) Induction motors drive.

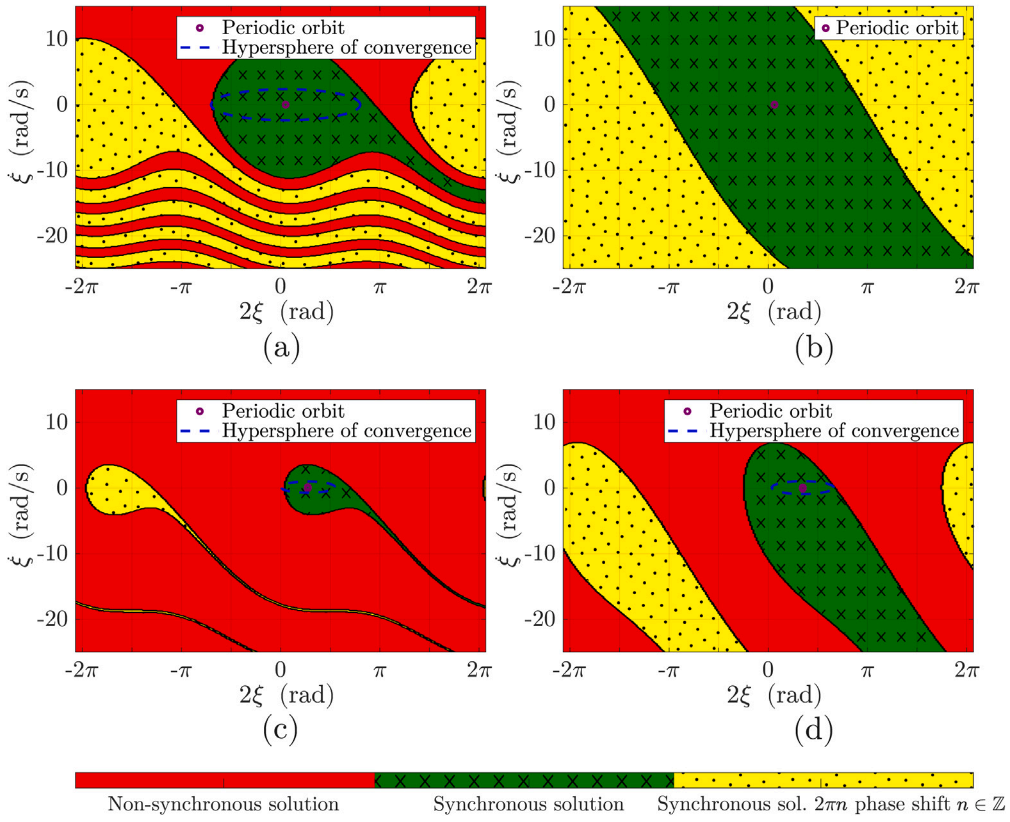

Fig. 12. Basins of attraction of the synchronous motion in case of average supplied voltage $U_{\mathrm{avg}} = 400$ V for: (a) DC motor drive with voltage difference of $U_{\mathrm{diff}} = 40$ V. (b) Induction motor drive with voltage difference of $U_{\mathrm{diff}} = 40$ V. (c) DC motor drive with voltage difference of $U_{\mathrm{diff}} = 200$ V. (d) Induction motor drive with voltage difference of $U_{\mathrm{diff}} = 200$ V.

solution and of the hypersphere of convergence derived from the LIM were also added to the figures. As the voltage difference increases, a clear reduction in the area of the basin of attraction is observed for both motor types, which was expected considering the trend of the LIM. In the figures, the solutions with the phase differences offset by 2π are treated as distinct attractive periodic orbits; however, from an engineering standpoint, they represent the same steady-state behavior differing only in their transient characteristics. From this perspective, the existence of the globally stable region is clearly observable for the induction motor drive with $U_{\mathrm{diff}} = 40$ V voltage difference, as all initial conditions converge to a synchronous periodic orbit under these conditions. The fact that the hypersphere of convergence section is very close to the basin of attraction boundary suggests that the algorithm provides a good approximation of the LIM. Additionally, the fact that, in some cases, the hypersphere of convergence slightly exceeds the actual size of the basin of attraction demonstrates that the computed LIM is an upper estimate of its actual value. It also shows that the hypersphere does not uniformly cover the basin of attraction; however, since the change in their sizes happens in a similar manner, with the calculation of the hypersphere the development of the basin's extent can be tracked sufficiently. In this case, the boundary of the basin of attraction is not far from the hypersphere's perimeter, making the computation of the local integrity measure a good approach to approximate the basin's size from an engineering standpoint. As a final comment, we note that, although the computation of the whole basin of attraction provides much more information regarding the system's robustness, computing the 10-dimensional basin of attraction is computationally unfeasible for the system under study, and even obtaining a single section is several order of magnitude more expensive than computing the LIM. Accordingly, a direct analysis of the basin of attraction does not allow to perform a parametric analysis as the one in Fig. 10.

5. Conclusion

In this paper, a mathematical model was developed for the dynamics of a self-synchronizing vibratory screen with two unbalanced mass exciters driven by two different motors types. Based on the mechanical models for DC motor and induction motor drives, their stability diagrams were analytically computed using the averaging method; direct numerical simulations confirmed the analytical results with remarkable accuracy. The analysis revealed, that for both motor types, there exists a bistable parameter region, defined in terms of supplied voltages, where a stable synchronous state and a stable non-synchronous state coexist. Although the DC motor leads to a larger stable region for synchronous motion, making it appear to be the more convenient choice, the bistable region is notably smaller for the induction motor drive, which enhances its safety.

Since the synchronous motion is only locally stable in the bistable region, its robustness against external perturbations was evaluated using the `DynIn` toolbox [26,28] to directly estimate the local integrity measure of the periodic synchronous solution. The results indicate, that in regions where synchronized motion is not globally stable, the dynamical integrity decreases very rapidly, posing a risk to reliable operation for both motor types. However, the induction motor-driven system exhibits a significantly larger globally stable region for synchronous operation, making it a preferable choice from this aspect of the operation.

Overall, this study highlights the importance of evaluating the dynamical integrity of synchronous motions as a complement to stability analysis. Although stability analysis suggests that the DC motor provides a larger stable region for synchronous motion than the induction motor, the dynamical integrity analysis reveals that a large part of this stable region is unsafe for real applications because of its very low dynamical integrity. Accordingly, despite the stability analysis results, the induction motor drive remains the preferred choice for ensuring robust and stable operation of the vibratory screen.

CRediT authorship contribution statement

Márton Szabó: Writing – original draft, Investigation. **Ákos Miklós:** Writing – review & editing, Supervision. **Giuseppe Habib:** Writing – review & editing, Supervision.

Declaration of Generative AI and AI-assisted technologies in the writing process

During the preparation of this work the authors used ChatGPT/4o in order to improve language and readability. After using this tool/service, the authors reviewed and edited the content as needed and take full responsibility for the content of the publication.

Declaration of competing interest

The authors declare that they have no known competing financial interests or personal relationships that could have appeared to influence the work reported in this paper.

Acknowledgments

The project supported by the Doctoral Excellence Fellowship Programme (DCEP) is funded by the National Research Development and Innovation Fund of the Ministry of Culture and Innovation and the Budapest University of Technology and Economics.

Giuseppe Habib acknowledge the financial support of the Committee of Science and Technology of Shanghai, China (Grant No. 24160712200).

Appendix A. Mechanical model

Displacements of the springs and their time derivatives:

$$x_A = x - a\cos(\alpha+\varphi) + c\sin(\alpha+\varphi) + a\cos\alpha - c\sin\alpha \tag{A.1}$$

$$x_B = x + b\cos(\alpha+\varphi) - c\sin(\alpha+\varphi) - b\cos\alpha - c\sin\alpha \tag{A.2}$$

$$y_A = y - a\sin(\alpha+\varphi) - c\cos(\alpha+\varphi) + c\cos\alpha + a\sin\alpha \tag{A.3}$$

$$y_B = y + b\sin(\alpha+\varphi) - c\cos(\alpha+\varphi) + c\cos\alpha - b\sin\alpha \tag{A.4}$$

$$\dot{x}_A = \dot{x} + \dot{\varphi}\,[c\cos(\alpha+\varphi) + a\sin(\alpha+\varphi)] \tag{A.5}$$

$$\dot{x}_B = \dot{x} + \dot{\varphi}\,[c\cos(\alpha+\varphi) - b\sin(\alpha+\varphi)] \tag{A.6}$$

$$\dot{y}_A = \dot{y} + \dot{\varphi}\,[c\sin(\alpha+\varphi) - a\cos(\alpha+\varphi)] \tag{A.7}$$

$$\dot{y}_B = \dot{y} + \dot{\varphi}\,[c\sin(\alpha+\varphi) + b\cos(\alpha+\varphi)] \tag{A.8}$$

Equations of motion:

$$\begin{aligned}
&(M+m_1+m_2)\ddot{x} + (c_{xA}+c_{xB})\dot{x} + (k_{xA}+k_{xB})x \\
&+ \left[c(c_{xA}+c_{xB})\cos(\alpha+\varphi) + ac_{xA}\sin(\alpha+\varphi) + bc_{xB}\sin(\alpha+\varphi)\right]\dot{\varphi} \\
&+ (bk_{xB}-ak_{xA})\cos(\alpha+\varphi) + c(k_{xA}+k_{xB})\sin(\alpha+\varphi) \\
&+ (ak_{xA}-bk_{xB})\cos(\alpha) + c(k_{xA}+k_{xB})\sin(\alpha) = \\
&= m_1r_1\dot{\varphi}^2\cos(\alpha+\beta_1+\varphi) + m_2r_2\dot{\varphi}^2\cos(\alpha+\beta_2+\varphi) \\
&+ m_1r_1\ddot{\varphi}\sin(\alpha+\beta_1+\varphi) + m_2r_2\ddot{\varphi}\sin(\alpha+\beta_2+\varphi) \\
&+ e_1m_1\cos(\vartheta_1)\dot{\vartheta}_1^{\,2} - e_2m_2\cos(\vartheta_2)\dot{\vartheta}_2^{\,2} \\
&+ e_1m_1\sin(\vartheta_1)\ddot{\vartheta}_1 - e_2m_2\sin(\vartheta_2)\ddot{\vartheta}_2
\end{aligned} \tag{A.9}$$

$$\begin{aligned}
&(M+m_1+m_2)\ddot{y} + (c_{yA}+c_{yB})\dot{y} + (k_{yA}+k_{yB})y \\
&+ \left[c(c_{yA}+c_{yB})\sin(\alpha+\varphi) - ac_{yA}\cos(\alpha+\varphi) + bc_{yB}\cos(\alpha+\varphi)\right]\dot{\varphi} \\
&+ (bk_{yB}-ak_{yA})\sin(\alpha+\varphi) - c(k_{yA}+k_{yB})\cos(\alpha+\varphi) \\
&+ (ak_{yA}-bk_{yB})\sin(\alpha) + c(k_{yA}+k_{yB})\cos(\alpha) = \\
&= m_1r_1\dot{\varphi}^2\sin(\alpha+\beta_1+\varphi) + m_2r_2\dot{\varphi}^2\sin(\alpha+\beta_2+\varphi) \\
&- m_1r_1\ddot{\varphi}\cos(\alpha+\beta_1+\varphi) - m_2r_2\ddot{\varphi}\cos(\alpha+\beta_2+\varphi) \\
&+ (M+m_1+m_2)g + e_1m_1\sin(\vartheta_1)\dot{\vartheta}_1^{\,2} + e_2m_2\sin(\vartheta_2)\dot{\vartheta}_2^{\,2} \\
&- e_1m_1\cos(\vartheta_1)\ddot{\vartheta}_1 - e_2m_2\cos(\vartheta_2)\ddot{\vartheta}_2
\end{aligned} \tag{A.10}$$

$$\begin{aligned}
&(J+m_1r_1^2+m_2r_2^2)\ddot{\varphi} + \big\{c_{xA}(c\cos(\alpha+\varphi) + a\sin(\alpha+\varphi))^2 \\
&+ c_{xB}(c\cos(\alpha+\varphi) - b\sin(\alpha+\varphi))^2 + c_{yA}(a\cos(\alpha+\varphi) \\
&- c\sin(\alpha+\varphi))^2 + c_{yB}(b\cos(\alpha+\varphi) + c\sin(\alpha+\varphi))^2 \\
&+ \big[c_{xA}(c\cos(\alpha+\varphi) + a\sin(\alpha+\varphi)) + c_{xB}(c\cos(\alpha+\varphi)) \\
&-c_{xB}(b\sin(\alpha+\varphi))\big]\,\dot{x} + \big[-c_{yA}(a\cos(\alpha+\varphi) - c\sin(\alpha+\varphi)) \\
&+c_{yB}(b\cos(\alpha+\varphi) + c\sin(\alpha+\varphi))\big]\,\dot{y}\big\}\,\dot{\varphi} \\
&+ k_{xA}(c\cos(\alpha+\varphi) - b\sin(\alpha+\varphi))(c\sin(\alpha+\varphi) - a\cos(\alpha+\varphi)) \\
&+ k_{xA}(c\cos(\alpha+\varphi) - b\sin(\alpha+\varphi))(a\cos(\alpha) - c\sin(\alpha)) \\
&+ k_{xB}(c\cos(\alpha+\varphi) + a\sin(\alpha+\varphi))(c\sin(\alpha+\varphi) + b\cos(\alpha+\varphi)) \\
&- k_{xB}(c\cos(\alpha+\varphi) + a\sin(\alpha+\varphi))(b\cos(\alpha) + c\sin(\alpha)) \\
&+ k_{yA}(a\cos(\alpha+\varphi) - c\sin(\alpha+\varphi))(a\sin(\alpha+\varphi) + c\cos(\alpha+\varphi)) \\
&- k_{yA}(a\cos(\alpha+\varphi) - c\sin(\alpha+\varphi))(c\cos(\alpha) + a\sin(\alpha)) \\
&+ k_{yB}(b\cos(\alpha+\varphi) + c\sin(\alpha+\varphi))(b\sin(\alpha+\varphi) - c\cos(\alpha+\varphi)) \\
&+ k_{yB}(b\cos(\alpha+\varphi) + c\sin(\alpha+\varphi))(c\cos(\alpha) - b\sin(\alpha)) \\
&+ \left[(k_{xA}+k_{xB})c\cos(\alpha+\varphi) + (k_{xA}a - k_{xB}b)\sin(\alpha+\varphi)\right]x \\
&+ \left[(k_{yA}+k_{yB})c\sin(\alpha+\varphi) - (k_{yA}a - k_{yB}b)\cos(\alpha+\varphi)\right]y = \\
&= (m_1r_1\sin(\alpha+\beta_1+\varphi) + m_2r_2\sin(\alpha+\beta_2+\varphi))\ddot{x} \\
&- (m_1r_1\cos(\alpha+\beta_1+\varphi) + m_2r_2\cos(\alpha+\beta_2+\varphi))\ddot{y} \\
&- e_1m_1r_1\left[\sin(\alpha+\beta_1+\varphi-\vartheta_1)\dot{\vartheta}_1^{\,2} + \cos(\alpha+\beta_1+\varphi-\vartheta_1)\ddot{\vartheta}_1\right] \\
&+ e_2m_2r_2\left[\sin(\alpha+\beta_2+\varphi+\vartheta_2)\dot{\vartheta}_2^{\,2} - \cos(\alpha+\beta_2+\varphi+\vartheta_2)\ddot{\vartheta}_2\right]
\end{aligned} \tag{A.11}$$

$$\begin{aligned}
&m_1e_1^2\ddot{\vartheta}_1 - m_1e_1\sin(\vartheta_1)\ddot{x} + m_1e_1r_1\cos(\alpha+\beta_1+\varphi-\vartheta_1)\ddot{\varphi} \\
&+ m_1e_1\cos(\vartheta_1)\ddot{y} - m_1e_1r_1\sin(\alpha+\beta_1+\varphi-\vartheta_1)\dot{\varphi}^2 = T_1
\end{aligned} \tag{A.12}$$

$$\begin{aligned}
&m_2e_2^2\ddot{\vartheta}_2 - m_2e_2\sin(\vartheta_2)\ddot{x} + m_2e_2r_2\cos(\alpha+\beta_2+\varphi-\vartheta_2)\ddot{\varphi} \\
&+ m_2e_2\cos(\vartheta_2)\ddot{y} - m_2e_2r_2\sin(\alpha+\beta_2+\varphi-\vartheta_2)\dot{\varphi}^2 = T_2
\end{aligned} \tag{A.13}$$

Appendix B. Parameters in Eq. (15)

$$
\begin{aligned}
&\mathbf{A}=\begin{bmatrix} a_{11} & a_{12} & 0\\ a_{21} & a_{22} & 0\\ 0 & 0 & 1\end{bmatrix},\mathbf{B}=\begin{bmatrix} b_{11} & b_{12} & 0\\ b_{21} & b_{22} & 0\\ 0 & \overline{\omega}_m & 0\end{bmatrix},\boldsymbol{\varepsilon}=\begin{bmatrix}\overline{\varepsilon}_1\\ \overline{\varepsilon}_2\\ \overline{\xi}\end{bmatrix},\mathbf{u}=\begin{bmatrix}u_1\\ u_2\\ 0\end{bmatrix}\\
a_{11} =&\eta_1 e_1^2+\eta_2 e_2^2+\frac{1}{2}\left[\eta_1^2 e_1^2 W_{cs1}+\eta_2^2 e_2^2 W_{cs2}\right]\\
&-\eta_1\eta_2 e_1 e_2(a_{cs}\cos(2\xi)+b_{cs}\sin(2\xi))\\
a_{12} =&\eta_1 e_1^2-\eta_2 e_2^2+\frac{1}{2}\left[\eta_1^2 e_1^2 W_{cs1}-\eta_2^2 e_2^2 W_{cs2}\right]\\
&-\eta_1\eta_2 e_1 e_2(a_{ss}\sin(2\xi)+b_{ss}\cos(2\xi))\\
a_{21} =&\eta_1 e_1^2-\eta_2 e_2^2+\frac{1}{2}\left[\eta_1^2 e_1^2 W_{cs1}-\eta_2^2 e_2^2 W_{cs2}\right]\\
&+\eta_1\eta_2 e_1 e_2(a_{ss}\sin(2\xi)+b_{ss}\cos(2\xi))\\
a_{22} =&\eta_1 e_1^2+\eta_2 e_2^2+\frac{1}{2}\left[\eta_1^2 e_1^2 W_{cs1}+\eta_2^2 e_2^2 W_{cs2}\right]\\
&+2\eta_1\eta_2 e_1 e_2(a_{cs}\cos(2\xi)+b_{cs}\sin(2\xi))\\
b_{11} =&-\frac{f_1+f_2}{M_t}-\frac{k_1+k_2}{M_t\overline{\omega}_m}-\overline{\omega}_m\left[\eta_1^2 e_1^2 W_{ss1}+\eta_2^2 e_2^2 W_{ss2}\right]\\
&+2\overline{\omega}_m\eta_1\eta_2 e_1 e_2(a_{ss}\cos(2\xi)+b_{ss}\sin(2\xi))\\
b_{12} =&-\frac{f_1-f_2}{M_t}-\frac{k_1-k_2}{M_t\overline{\omega}_m}-\overline{\omega}_m\left[\eta_1^2 e_1^2 W_{ss1}-\eta_2^2 e_2^2 W_{ss2}\right]\\
&-2\overline{\omega}_m\eta_1\eta_2 e_1 e_2(a_{cs}\sin(2\xi)+b_{cs}\cos(2\xi))\\
b_{21} =&-\frac{f_1-f_2}{M_t}-\frac{k_1-k_2}{M_t\overline{\omega}_m}-\overline{\omega}_m\left[\eta_1^2 e_1^2 W_{ss1}-\eta_2^2 e_2^2 W_{ss2}\right]\\
&+2\eta_1\eta_2 e_1 e_2(a_{cs}\sin(2\xi)+b_{cs}\cos(2\xi))\\
b_{22} =&-\frac{f_1+f_2}{M_t}-\frac{k_1+k_2}{M_t\overline{\omega}_m}-\overline{\omega}_m\left[\eta_1^2 e_1^2 W_{ss1}+\eta_2^2 e_2^2 W_{ss2}\right]\\
&-2\eta_1\eta_2 e_1 e_2(a_{ss}\cos(2\xi)+b_{ss}\sin(2\xi))
\end{aligned}
\tag{B.1}
$$

$$
\begin{aligned}
u_1 =&\frac{T_{10}+T_{20}}{M_t\overline{\omega}_m}-\frac{f_1+f_2}{M_t}-\frac{\overline{\omega}_m}{2}\left[\eta_1^2 e_1^2 W_{ss1}+\eta_2^2 e_2^2 W_{ss2}\right]\\
&+\overline{\omega}_m\eta_1\eta_2 e_1 e_2(a_{ss}\cos(2\xi)+b_{ss}\sin(2\xi))\\
u_2 =&\frac{T_{10}-T_{20}}{M_t\overline{\omega}_m}-\frac{f_1-f_2}{M_t}-\frac{\overline{\omega}_m}{2}\left[\eta_1^2 e_1^2 W_{ss1}-\eta_2^2 e_2^2 W_{ss2}\right]\\
&-\overline{\omega}_m\eta_1\eta_2 e_1 e_2(a_{cs}\sin(2\xi)+b_{cs}\cos(2\xi))\\
W_{cs1} =&\mu_x\cos\delta_x+\mu_y\cos\delta_y+\frac{r_1^2}{l_e^2}\mu_\varphi\cos\delta_\varphi\\
W_{ss1} =&\mu_x\sin\delta_x+\mu_y\sin\delta_y+\frac{r_1^2}{l_e^2}\mu_\varphi\sin\delta_\varphi\\
W_{cs2} =&\mu_x\cos\delta_x+\mu_y\cos\delta_y+\frac{r_2^2}{l_e^2}\mu_\varphi\cos\delta_\varphi\\
W_{ss2} =&\mu_x\sin\delta_x+\mu_y\sin\delta_y+\frac{r_2^2}{l_e^2}\mu_\varphi\sin\delta_\varphi\\
a_{cs} =&\mu_x\cos\delta_x-\mu_y\cos\delta_y-\frac{r_1 r_2}{l_e^2}\cos(2\alpha+\beta_1+\beta_2)\mu_\varphi\cos\delta_\varphi\\
a_{ss} =&\mu_x\sin\delta_x-\mu_y\sin\delta_y-\frac{r_1 r_2}{l_e^2}\cos(2\alpha+\beta_1+\beta_2)\mu_\varphi\sin\delta_\varphi\\
b_{cs} =&\frac{r_1 r_2}{l_e^2}\sin(2\alpha+\beta_1+\beta_2)\mu_\varphi\cos\delta_\varphi\\
b_{ss} =&\frac{r_1 r_2}{l_e^2}\sin(2\alpha+\beta_1+\beta_2)\mu_\varphi\sin\delta_\varphi
\end{aligned}
$$

In the case of direct current motors the parameter of the driving torque:

$$T_{i0} = \frac{n_m K_t}{R_a} U_i, k_i \quad = 0, f_i \quad = n_m \left(\frac{K_t K_E}{R_a} + c_i \right), i = 1, 2 \tag{B.2}$$

In the case of induction motors the parameter of the driving torque:

$$\begin{aligned} T_{i0} &= \frac{3n_m}{\omega_s} \cdot \frac{\frac{R_r}{s_i}}{\left[R_s \left(\frac{L_m}{L_s+L_m} \right)^2 + \frac{R_r}{s_i} \right]^2 + (L_s + L_r)^2} \cdot \left(\frac{L_m}{L_s + L_m} \right)^2 \cdot U_i^2 \\ k_i &= \frac{\overline{\omega}_m}{\omega_s - \overline{\omega}_m} T_{i0} - \frac{3n_m L_m^2 R_r U_i^2}{(L_m + L_s)^2} \left[\frac{2R_r^2 \overline{\omega}_m}{s_i^2} + \frac{2L_m^2 R_r R_s \overline{\omega}_m}{(L_m + L_s)^2 s_i} \right] \\ f_i &= c_i, \qquad i = 1, 2 \end{aligned} \tag{B.3}$$

Data availability

No data was used for the research described in the article.

References

[1] I.I. Blekhman, Synchronization in Science and Technology, ASME Press, New York, USA, 1988.

[2] C. Huygens, Horologium Oscillatorium, Apud F. Muguet, Paris, France, 1673.

[3] I.I. Blekhman, B.P. Lavrov, On an integral criterion for stability of motion, J. Appl. Math. Mech. 24 (5) (1960) 1416–1422, http://dx.doi.org/10.1016/0021-8928(60)90122-2.

[4] I.I. Blekhman, A.L. Fradkov, O.P. Tomchina, D.E. Bogdanov, Self-synchronization and controlled synchronization: general definition and example design, Math. Comput. Simulation 58 (4) (2002) 367–384, http://dx.doi.org/10.1016/S0378-4754(01)00378-0.

[5] M. Paz, J.D. Cole, Self-synchronization of two unbalanced rotors, J. Vib. Acoust. 114 (1) (1992) 37–41, http://dx.doi.org/10.1115/1.2930230.

[6] Q. Han, B. Wen, Stability and bifurcation of self-synchronization of a vibratory screener excited by two eccentric motors, Adv. Theor. Appl. Mech. 1 (3) (2008) 107–119.

[7] B. Wen, L.Z. Guan, Synchronization theory of self-synchronous vibratory machines with two asymmetrical vibrators, in: Proceedings of International Conference on Mechanical Dynamics, Shenyang, 1987, pp. 434–439.

[8] C. Zhao, H. Zhu, R. Wang, B. Wen, Synchronization of two non-identical coupled exciters in a non-resonant vibrating system of linear motion. Part I: Theoretical analysis, Shock. Vib. 16 (2009) 505–515, http://dx.doi.org/10.3233/SAV-2009-0484.

[9] C. Zhao, H. Zhu, R. Wang, B. Wen, Synchronization of two non-identical coupled exciters in a non-resonant vibrating system of linear motion. Part II: Numerical analysis, Shock. Vib. 16 (2009) 517–528, http://dx.doi.org/10.3233/SAV-2009-0485.

[10] M. Du, Y. Hou, C. Yu, W. Wang, D. Hou, G. Xiong, Experimental investigation on synchronization of two co-rating rotors coupled with nonlinear springs, IEEE Access 8 (2020) 48226–48240, http://dx.doi.org/10.1109/ACCESS.2020.2975590.

[11] P. Fang, H. Peng, D. Changcheng, M. Zou, D. Hou, M. Du, G. chai, Synchronous state of unbalanced rotors in a three-dimensional space and far-resonance system, Proc. Inst. Mech. Eng. Part E: J. Process. Mech. Eng. 234 (1) (2020) 108–122, http://dx.doi.org/10.1177/0954408919889416.

[12] R. Peng, P. Fang, L. Yang, N. Chen, X. Zhao, Theoretical and experimental study for implementation of the elliptical trajectory in dual-motor vibration system, Proc. Inst. Mech. Eng. Part K: J. Multi-Body Dyn. 237 (2) (2023) 307–324, http://dx.doi.org/10.1177/14644193231173025.

[13] T. Zhang, B. Wen, J. Fan, Study on synchronization of two eccentric rotors driven by hydraulic motors in one vibrating system, Shock. Vib. 4 (1997) 305–310, http://dx.doi.org/10.3233/SAV-1997-45-602.

[14] X. Zhang, B. Wen, C. Zhao, Synchronization of three non-identical coupled exciters with the same rotating directions in a far-resonant vibrating system, J. Sound Vib. 332 (9) (2013) 2300–2317, http://dx.doi.org/10.1016/j.jsv.2012.12.003.

[15] G. Rega, S. Lenci, Identifying, evaluating, and controlling dynamical integrity measures in non-linear mechanical oscillators, Nonlinear Anal. 63 (5) (2005) 902–914, http://dx.doi.org/10.1016/j.na.2005.01.084.

[16] M. Stender, N. Hoffmann, bSTAB: an open-source software for computing the basin stability of multi-stable dynamical systems, Nonlinear Dynam. 107 (2022) 1451–1468, http://dx.doi.org/10.1007/s11071-021-06786-5.

[17] H. Mori, M. Sueda, K. Shiroshita, T. Kondou, Effect of damping and rotor moment of inertia on stability of self-synchronization for two unbalanced rotors, J. Sound Vib. 570 (2024) 118103, http://dx.doi.org/10.1016/j.jsv.2023.118103.

[18] M. Kapitaniak, K. Czolczynski, P. Perlikowski, A. Stefanski, T. Kapitaniak, Synchronous states of slowly rotating pendula, Phys. Rep. 541 (1) (2014) 1–44, http://dx.doi.org/10.1016/j.physrep.2014.02.008.

[19] I. Grinberg, O.V. Gendelman, Boundary for complete set of attractors for forced–damped essentially nonlinear systems, J. Appl. Mech. 82 (5) (2015) 051004, http://dx.doi.org/10.1115/1.4030045.

[20] A. Genda, A. Fidlin, O. Gendelman, The level-crossing problem of a weakly damped particle in quadratic potential well under harmonic excitation, Nonlinear Dynam. 111 (22) (2023) 20563–20578, http://dx.doi.org/10.1007/s11071-023-08875-z.

[21] V. Settimi, G. Rega, Global dynamics and integrity in noncontacting atomic force microscopy with feedback control, Nonlinear Dynam. 86 (2016) 2261–2277, http://dx.doi.org/10.1007/s11071-016-2620-9.

[22] C. Hsu, A theory of cell-to-cell mapping dynamical systems, J. Appl. Mech. 47 (4) (1980) 931–939, http://dx.doi.org/10.1115/1.3153816.

[23] P. Belardinelli, S. Lenci, An efficient parallel implementation of cell mapping methods for M DOF systems, Nonlinear Dynam. 86 (2016) 2279–2290, http://dx.doi.org/10.1007/s11071-016-2849-3.

[24] J.M.T. Thompson, Chaotic phenomena triggering the escape from a potential well, Proc. R. Soc. Lond. Ser. A, Math. Phys. Sci. 421 (1861) (1989) 195–225, http://dx.doi.org/10.1098/rspa.1989.0009.

[25] M.S. Soliman, J.M.T. Thompson, Integrity measures quantifying the erosion of smooth and fractal basins of attraction, J. Sound Vib. 135 (1989) 453–475, http://dx.doi.org/10.1016/0022-460X(89)90699-8.

[26] G. Habib, Dynamical integrity assessment of stable equilibria: a new rapid iterative procedure, Nonlinear Dynam. 106 (2021) 2073–2096, http://dx.doi.org/10.1007/s11071-021-06936-9.

[27] B. Szaksz, G. Stepan, G. Habib, Dynamical integrity estimation in time delayed systems: a rapid iterative algorithm, J. Sound Vib. 571 (2024) 118045, http://dx.doi.org/10.1016/j.jsv.2023.118045.

[28] D. Patkó, G. Habib, Dynamical integrity of periodic orbits: A computationally efficient approach, Nonlinear Dynam. (2025) http://dx.doi.org/10.1007/s11071-025-11424-5.

[29] Á. Miklós, Z. Szabó, Simulation and experimental validation of the dynamical model of a dual-rotor vibrotactor, J. Sound Vib. 334 (2015) 98–107, http://dx.doi.org/10.1016/j.jsv.2014.06.011.

[30] S.J. Chapman, Electric Machinery and Power System Fundamentals, McGraw-Hill Education, New York, USA, 2002.

[31] Gama Motors, MP160L DC motor, 2025, https://ek.ck.ua/en/electric-motor-of-a-direct-current-mp160l/. (Accessed 16 April 2025).

[32] ABB Group, M3BP 225SMA 4 IE4 induction motor, 2025, https://www.abb.com/global/en/products/3gbp222220-bek. (Accessed 9 September 2025).

[33] I.B. Shiroky, O.V. Gendelman, Modal synchronization of coupled bistable van der pol oscillators, Chaos Solitons Fractals 143 (2021) 110555, http://dx.doi.org/10.1016/j.chaos.2020.110555.

[34] Y. Wolfovich, O.V. Gendelman, Modal and wave synchronization in coupled self-excited oscillators, Chaos: Interdiscip. J. Nonlinear Sci. 35 (2) (2025) 023139, http://dx.doi.org/10.1063/5.0250314.